5.1. Introduction

Environmental degradation and ecological imbalances have significantly increased as a result of the tremendous demands for resource exploitation brought about by industrialization. The relentless pursuit of industrial and technical progress has released a torrent of toxins into our surroundings, endangering the fragile equilibrium of ecosystems. Many different types of pollutants, including metallic, inorganic, organic, inorganic, and physical pollutants, continue to have a negative impact on aquatic and terrestrial ecosystems [1]. The primary causes of these pollutants are numerous human activities, including mining, agricultural runoffs, automobile emissions, industrial waste, etc. [2]. If the amount of heavy metals in the air, water, or soil is more than a certain threshold, they may be considered hazardous pollutants and have a tendency to bind covalently with organic substances. More specifically, when heavy metal ions enter the human body, they tend to accumulate with live cells and can result in major health problems [3]. Even though some heavy metals are essential for biological functioning in living organisms they show toxic adversity beyond critical dose and long-term exposure [4]. However, non-essential heavy metals such as Cd, Pb, and Hg are harmful even at low concentrations when they build up in biota and promote the production of reactive oxygen species (ROS), which significantly impairs the antioxidant defense mechanism of cellular processes [5]. This illness eventually results in major health disorder such as central nervous system collapse, respiratory and circulatory system dysfunction, fatal cancer as well as multiple organ failure [6]. Therefore, proper monitoring, removal, and control of such contaminants is extremely crucial to ensure a safe, and healthy environment for the cause of livable planet.

Techniques like atomic emission spectroscopy, atomic fluorescence spectroscopy, atomic absorption spectroscopy and inductively coupled plasma mass spectroscopy, electrothermal atomic absorption spectroscopy etc. are already in use for detecting the heavy metals ions. However, these methods are limited by things like lengthy testing times, pricey equipment, and intricate measurement procedures. [4]. One of the most promising detection methods of this new era is electroanalytical technology, which offers great sensitivity, selectivity, portability, repeatability, and a very low limit of detection (LOD). For electroanalysis an electrochemical workstation is required where the reference electrodes are generally made of Ag/AgCl, counter electrodes made of platinum (Pt), and a working electrode made of Au, Pt, glassy carbon etc. [5]. Chemical reactions occur when any analyte comes into contact with the working electrode. As a result, current, potential, capacitance, and resistance may change abruptly and indicate that the injected analyte has been sensed. However, due to its limitations such as its low reaction rate and low number of active sites for reaction, bare working electrode is often not suited for sensing. Therefore, to greatly increase the sensitivity, the bare electrode can be modified using various materials such as polymers, carbon compounds, metal oxides, etc. [6].

Metal ions and micropores combine to form metal organic frameworks (MOF), a unique class of crystalline molecules. Since chemical sensors primarily rely on their surface activity and interactions, the MOF with well-developed porosity can be an excellent sensing material. [7]. These MOFs are well-organized systems with high porosity, high charge transfer, high crystallinity, high surface area etc. Because of its adaptability, the MOF has been used in a wide range of applications, including biomedical engineering, gas separation, gas storage, sensing, catalysis, and photovoltaics [8,9]. The majority of common MOFs have insulating properties, which limits their applicability in specific applications. These restrictions can be circumvented, though, by combining them with other conducting materials such as conducting polymer, metal NPs, graphene, porous carbon, etc. In the recent years, simultaneous detection of different heavy metal ions is a trending topic as it minimizes the cost and hardship of using several detectors one after another. Liu and his group have developed a co-assembly of Fe_3O_4 at magnetic mesoporous carbon for the detection of Hg^{2+} and Pb^{2+} through differential pulse stripping voltammetry (DPSV) technique [10]. Due to the availability, good performance in catalysis and biocompatibility iron-oxide materials are used in electrochemical sensing, another such work was carried out by Wu et al [11]. They used the Fe_3O_4 nanoparticles for Pb^{2+} and Cu^{2+} detection with lower limit of detection up to 9.48 nM and 38.31 nM. Another report of simultaneous detection with Hg^{2+} with a different metal ion was presented by Xiong et al. where they used phenolic resin-based carbon nanosphere [12]. High surface area, presence of redox active sites and flexibility to design with desired metal centers and linkers makes MOF a good candidate for simultaneous sensing. Some works such as Y. Ding's group carbonized the MOF UiO-66 and modified the glassy carbon electrode by the method of bismuth plating which they used for simultaneous detection of Cd and Pb

[13]. Lu et.al synthesized a UiO-66 composite with graphene aerogel for the simultaneous detection of more than two metal ions like Cu^{2+}, Cd^{2+}, Hg^{2+} and Pb^{2+} [14]. Combining MOF with other functional materials can give rise to a target specific sensor material for environmental contaminant sensing. Metal nanoparticles, or metal oxide nanoparticles (MONPs) play a crucial role in enhancing the conductivity as well as catalytic behavior when combined with MOFs. Different groups have employed UiO-66 as a platform to support MONPs owing to its exceptional stability and porous character [15]. A composite of Ag and UiO-66 was considered to catalyze the oxidation of styrene by the group of Li et al. [16]. In Cu-BTC MOF, Cu can replace Ag ions through post-synthetic exchange method which in turn enhances the catalysis of toluene [17]. In an effort to improve electrocatalytic performance using heavy metal ion detection, an Ag_2O decorated MOF has been developed in consideration of the quality-enhancing factor of Ag insertions. Given this, it is imperative to create a different but equally effective method for identifying heavy metal ions in the terrestrial or aquatic environment for long-term monitoring and repeated use.

Acknowledging UiO-66's sensing potential, a strategy to detect Hg^{2+} and Cd^{2+} individually as well as simultaneously by incorporating Ag_2O nanoparticles (NPs) into the framework has been adapted. Here MOF has provided the platform for stabilizing Ag_2O and easy capturing of analytes while Ag_2O NPs would perform the redox activities for sensing Hg^{2+} and Cd^{2+} [18]. This chapter discusses the assessment of adequate electrochemical performance through cyclic voltammetry (CV) and electrochemical impedance spectroscopy (EIS) of Ag_2O incorporated UiO-66 -S1(MOF) and S2(MOF). The electrochemical sensing of Hg^{2+} and Cd^{2+} via differential pulse stripping voltammetry (DPSV) studies are also discussed, along with relevent underlying mechanisms.

5.2 Electrochemical properties of S1(MOF) and S2(MOF) coated working electrode

The electrochemical performance of S1(MOF) and S2(MOF) coated in ITO glass have been evaluated through cyclic voltammetry (CV) and electrochemical impedance spectroscopy (EIS) studies.

5.2.1 Cyclic voltammetry

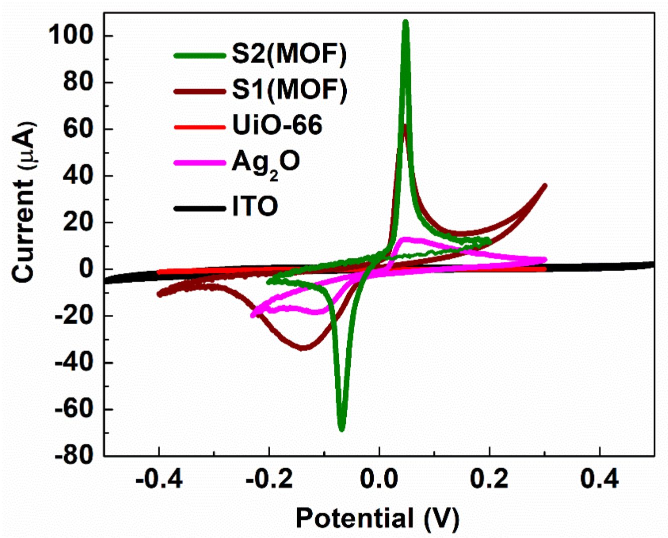

Fig. 5.1. Cyclic Voltammetry (CV) of bare ITO, UiO-66, Ag_2O, S1(MOF) and S2(MOF).

As for CV, 0.1 M PBS was employed as the electrolyte solution, Ag/AgCl as the reference electrode, platinum as the counter electrode for electrodes like bare ITO, UiO-66/ITO, Ag_2O/ITO and S1(MOF)/ITO and S2(MOF)/ITO, with a potential window of -0.5 V to +0.5 V (Fig. 5.1). The electrical insulating nature of the UiO-66 gives a CV response which is almost linear with the current response at nanoscale range along with non-obvious redox peaks. Even though ITO is conducting there was no redox reaction that would take place between the ITO and the components of PBS. The CVs of S1(MOF) and S2(MOF) possessed a reduction peak at -0.01 V that would correspond to reduction of Ag_2O to Ag and another stripping peak at 0.03 V resembles to further reduction of Ag. However, I_{pa} and I_{pc} of S2(MOF) have higher values than S1(MOF) which may be due to the presence of Ag_2O NPs on the surfaces of MOF with more exposed redox active sites. The peak-to-peak separation ($\Delta E= E_{pc}-E_{pa}$) for the respective samples is determined to be 113 mV and 182 mV which reveals the irreversibility of redox reactions being taken place between the PBS and the modified working electrodes [19].

The variation in cathodic (I_{pc}) and anodic peak (I_{pa}) currents with scan rate (v) for S1(MOF) and S2(MOF) systems can be found in Fig. 5.2. and 5.3. An increase in both I_{pc} and I_{pa} with increasing v has been realized in case of the former electrode. The *log-log* plots of I_p vs. v for S1(MOF) give two linear curves with different slopes. For the lower scan-rate up to 30 mV/s, an estimated slope of 0.79± 0.0015 and 1.15 ± 0.0118 has been observed for the forward and reverse scans, respectively. In contrast, a higher scan-rate offered the slopes as, 0.45 ± 0.0008 and 0.56 ± 0.0064 (Fig. 5.2. (b)). Thus, slopes for lower sweeps are closer to unity and for higher sweeps they are inclined to value 0.5 which is a clear indication of the presence of diffusion controlled as well as surface adsorbed processes in the reaction mechanism [20]. The result is accompanied by a linear plot of I_p vs. $v^{1/2}$ with a linear regression coefficient of 0.9988 and 0.9980 for anodic and cathodic peak currents, respectively. Randles-Sevcik equation fits to the plot by virtue of the diffusion process being dependent on surface area of the electrode and concentration of redox active sites [21]. The linear relationship between I_{pa} and I_{pc} with $v^{1/2}$ are given by the equations 5.1 and 5.2, shown in Fig. 5.2 (c). The linear part of scan-rate vs. peak

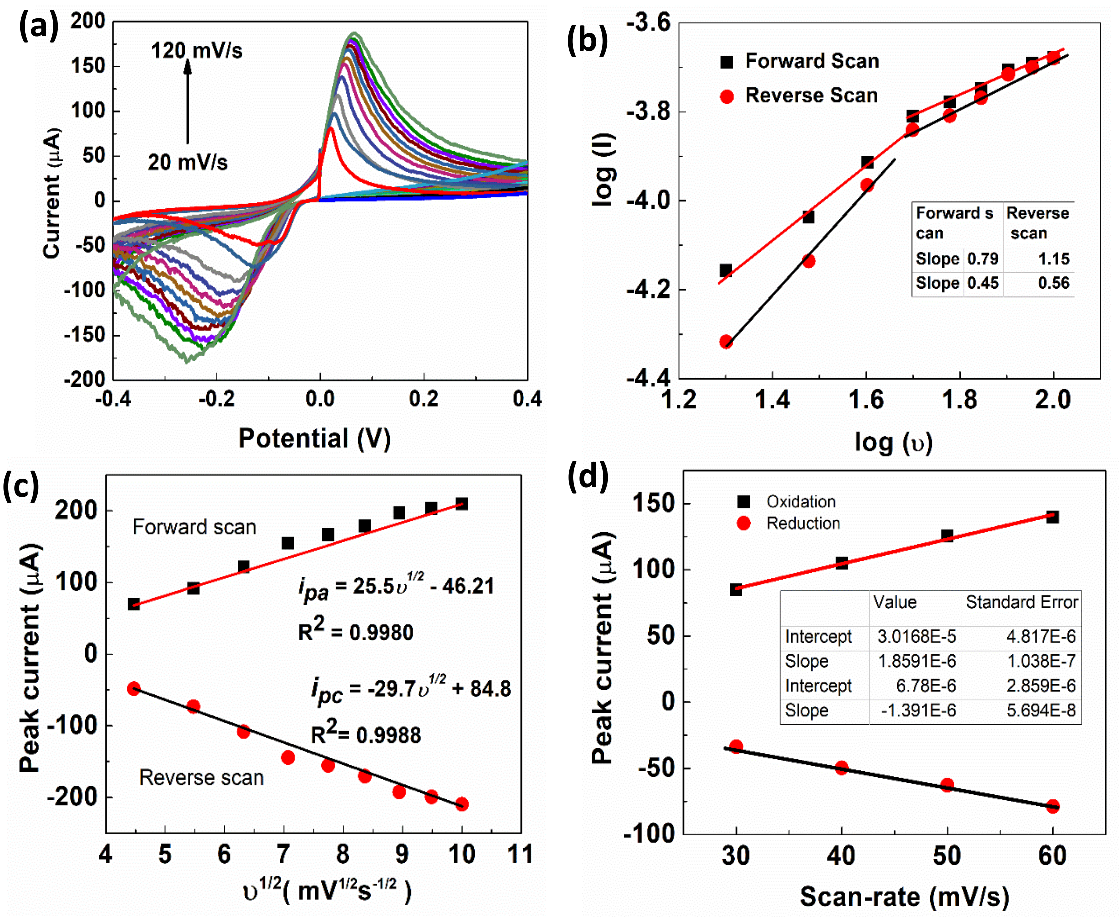

Fig. 5.2 CV of (a) S1(MOF) at different scan-rate from 20 mV/s to 120 mV/s (b) log-log plot of scan rate and peak current (c) linear response of square root of scan-rate vs. change in peak current (d) linear response of scan-rate vs. peak current for S1(MOF) .

current can be fitted with Brown-Anson equation [19] and concentration of redox active sites can be estimated from the slope of the trend (Fig. 5.2 (d)).

$$I_{pa}\,(\mu A) = 25.5 \times \upsilon^{1/2} - 46.21,\ R^2 = 0.9980 \quad (5.1)$$

$$I_{pc}\,(\mu A) = - 29.7 \times \upsilon^{1/2} + 84.8,\ R^2 = 0.9988 \quad (5.2)$$

Brown Anson equation can be written as-

$$I_p = \frac{n^2 F^2 I^* A}{4RT}\,\upsilon\ , \quad (5.3)$$

where, n is the number of electrons transferred during the reaction, F is the Faraday constant, A is the surface area of the electrode, υ is the scan rate, R is the gas constant and T is the absolute temperature and I^* is the surface concentration (mol/cm^2) [19]. Not surprisingly, the plot of scan-rate vs. peak current offered the linear trend from which the surface concentration of redox sites was estimated to be, ~1.96×10^{-9} mol/cm^2.

On the other hand, for S2(MOF), cathodic and anodic peaks are obtained at 0.04 mV and -0.077 mV and corresponding to the lowest scan-rate, 20 mV/s. As the scan-rate increases from 20 mV/s to 120 mV/s the peak currents were seen to improve observably. The *log-log* plots of I_p vs. v are like that of S1(MOF) systems as it showed two linear plots with slopes of 0.74± 0.046 and 0.81± 0.126 for lower scan rate and 0.36± 0.52 and 0.33± 0.286 for higher scan rate in forward and reverse sweeps, respectively (Fig. 5.3 (b)). Apparently, this material exhibited surface adsorption as well as diffusion-controlled phenomena at large. A shift in peak-to-peak separation was also witnessed with changing scan-rate, which indicated the quasi-reversibility of the reactions occurring at the surfaces. The linear relationship of I_p and $v^{1/2}$ are shown in Fig. 5.3 (c) and given by equation 5.4 and 5.5. By taking the slope of I_{pc} vs. v the surface concentration of redox active sites was determined to be, 6.4×10^{-9} mol/cm^2.

$$I_{pa}\,(\mu A) = 45.1 \times \upsilon^{1/2} + 11.7\ R^2 = 0.9985 \quad (5.4)$$

$$I_{pc}\,(\mu A) = -22.6 \times \upsilon^{1/2} - 66.1,\ R^2 = 0.9957 \quad (5.5)$$

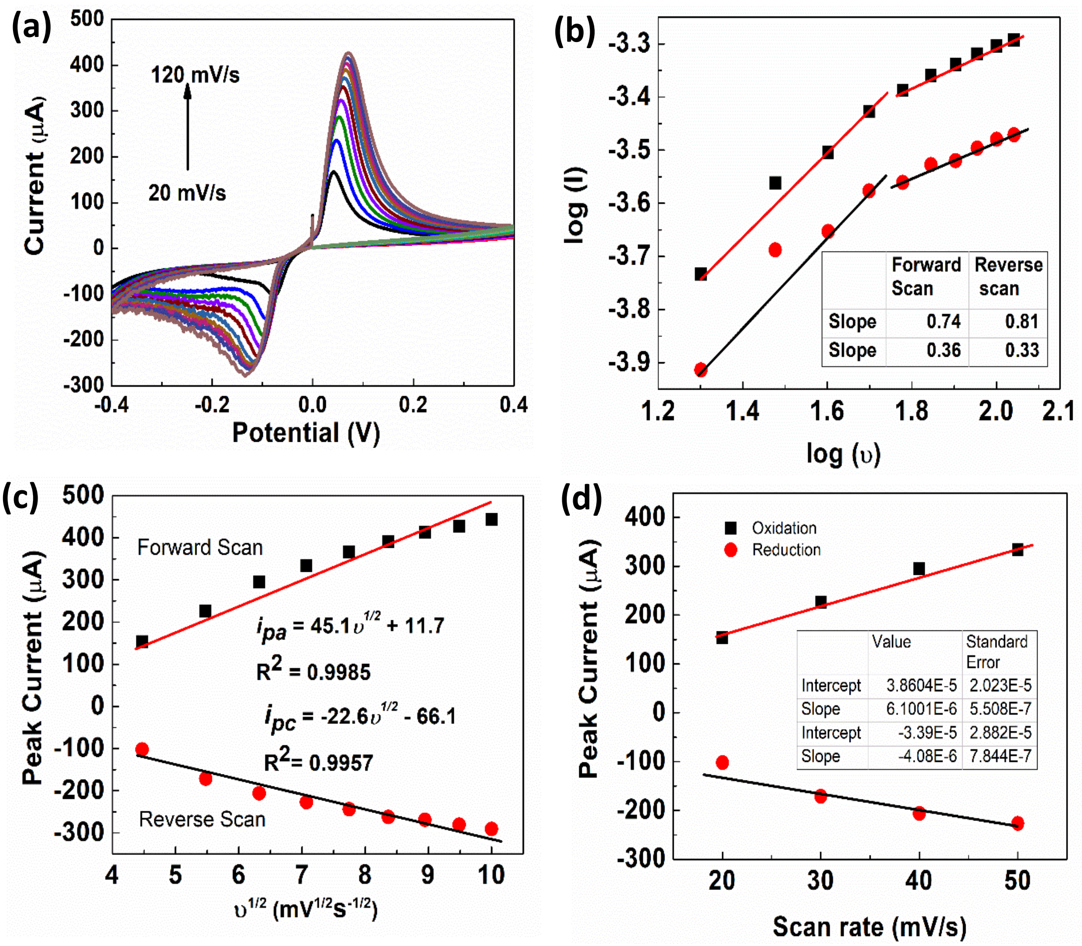

Fig .5.3 CV of (a) S1(MOF) at different scan-rate from 20 mV/s to 120 mV/s (b) *log-log* plot of scan rate and peak current (c) linear response of square root of scan-rate vs. change in peak current and (d) linear response of scan-rate vs. peak current for S2(MOF) electrode.

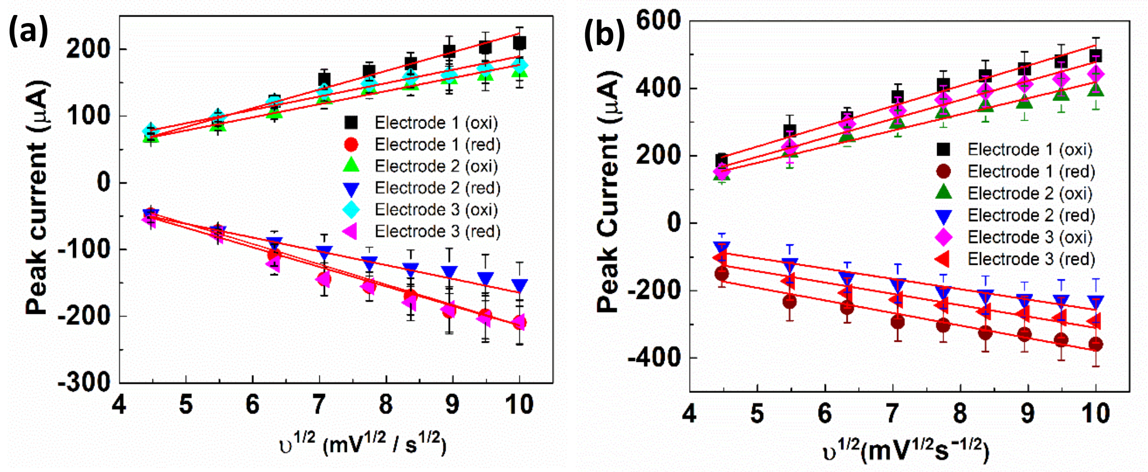

Fig .5.4 Linear-response of square-root of scan-rate and change in peak current of 3 different electrodes (a)S1(MOF) and (b) S2(MOF) with error bars.

Table 5.1 Summary of slope and intercept of linear plot of square root of scan-rate Vs. peak current of 3 different electrodes of S1(MOF) and S2(MOF).

Electrode	**1**		**2**		**3**	
S1(MOF)	**Anodic reaction**	**Cathodic reaction**	**Anodic reaction**	**Cathodic reaction**	**Anodic reaction**	**Cathodic reaction**
Intercept x 10^{-5}	-4.6214	8.4819	-1.1346	8.0076	-1.6724	9.8617
Slope x 10^{-5}	2.5572	-2.9708	1.7937	-2.0353	2.1336	-3.4539
Electrode	**1**		**2**		**3**	
S2(MOF)	**Anodic reaction**	**Cathodic reaction**	**Anodic reaction**	**Cathodic reaction**	**Anodic reaction**	**Cathodic reaction**
Intercept x 10^{-5}	1.1701	-6.618	2.2399	-10.678	3.3745	-1.8212
Slope x 10^{-5}	4.5147	-2.2698	6.5836	-3.8756	4.1871	-2.9719

The experiment was repeated for 3 different electrodes of S1(MOF) and S2(MOF) each to examine the reproducibility of the data. The linear plot highlighting change in peak current with increasing scan-rate for electrodes modified with S1(MOF) and S2(MOF) can be found in Fig. 5.3 (a) & (b). Results of the above experiments are tabulated in Table 5.1.

5.2.2 Electrochemical impedance spectroscopy (EIS)

To visualize the electron transfer effect upon modifying the ITO surface with MOFs, impedance spectroscopic measurements were considered. The EIS data of UiO-66, Ag_2O, S1(MOF), S2(MOF) were acquired in a 0.1 M PBS solution containing 0.5 M KCl and within a frequency range of 1 Hz to 1 MHz. In the Nyquist plot, shown in Fig. 5.5(a) the semicircular part in the higher frequency region represents the charge transfer controlled processes while at the lower frequency region the linear part corresponds to diffusion of the electroactive species. The diameter of the semicircle represents the charge transfer resistance (R_{ct}) at the electrode-electrolyte interface which is lowest for S2(MOF) as compared to the other materials (Table 5.2). It means electron transfer from S2(MOF) electrode to electrolyte becomes easier compared with the other electrodes. The UiO-66 with a high charge transfer resistance ($4.7 \times 10^3 \pm 183.7\ \Omega$) can depict its low electron transfer capability. As the Ag_2O NPs were loaded into the MOF, the semicircle declines while indicating the enhanced electron transfer capacity and redox activity of the electrodes. The plots were fitted to the circuit shown in Fig. 5.5(b) where R_s is the solution resistance offered by the electrolyte as depicted in the real axis of the Nyquist plot intercepting the semicircle. The resistance offered at the electrode-electrolyte interface at higher frequency is the R_{ct} which is parallel to the electric double layer (C_{dl}) capacitor. Accordingly, W is the Warburg impedance arises due to diffusion-limited processes at the electrode surface and is represented by a straight line in the lower frequency region of the Nyquist Plot [22]. Usually when the electrodes are made of heterogeneous interfaces like porous or composite material the capacitor formed at the electrode-electrolyte interface is not ideal. In such cases to quantify the non-ideal capacitive behaviour of the system a modelling element called constant phase element (CPE) is used. Here, in the equivalent circuit CPE1 is representing the depressed semicircle in the Nyquist plot. There also additional CPE2 and R1 are present in the circuit which may occur due to the capacitance formed at the interface of PEDOT and UiO-66.

All the parameters were calculated from the equivalent circuit and tabulated in Table 5.2. The R_{ct} value declines as the UiO-66 is decorated with semiconducting Ag_2O NPs reducing the barrier of current flow. On the other hand, electric double layer capacitor (C_{dl})values are also lowered in S1(MOF) and S2(MOF) systems because of reduction of specific surface area of UiO-66. As a result, they lose the capacity to hold charge eventually.

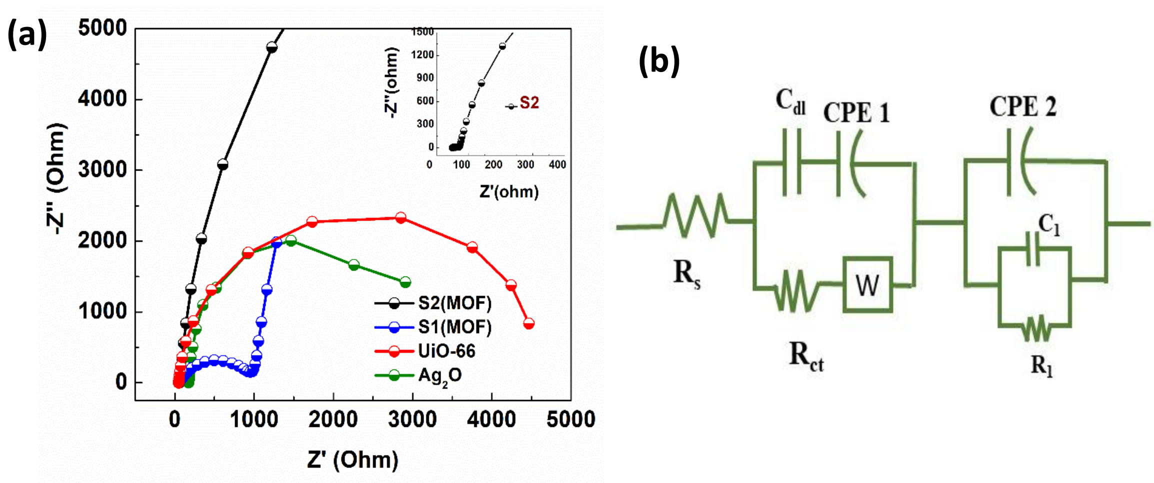

Fig. 5.5 (a) Nyquist plot of UiO-66, Ag_2O, S1(MOF), S2(MOF) in 0.5 M PBS (b) fitted model for the EIS patterns.

Table 5.2 EIS parameters obtained for different samples

Name	R_s **(Ω)**	R_{ct}**(Ω)**	C_{dl} **(F)** x10^{-9}	**CPE1** **S s^a**	W **S s$^{-1/2}$**	R_1**(Ω)**	C_1 **(F)** **× 10^{-6}**	**CPE2** **S s^a**
UiO-66	47.84	4750	7202	1.219 x 10^{-3}	121.4 x 10^{-3}	1.636	3.757	19.96 x 10^{-3}
Ag_2O	76.33	512.5	480.6	311.1 x 10^{-6}	67.51 x 10^{-3}	146.2	920.2	938.6 x 10^{-6}
S1 (MOF)	52.14	908.8	82.65	1.609 x 10^{-6}	886.7 x 10^{-6}	33.34	10.07	7.225 x 10^{-9}
S2 (MOF)	46.08	33.31	88.65	1.823 x 10^{-6}	589.7 x 10^{-6}	16.99	450.07	898.6 x 10^{-6}

5.3 Optimization of pH and deposition time

Optimization in the pH of the electrolyte, deposition voltage, accumulation time were done for the S1(MOF)/S2(MOF) coated ITO electrodes. The pH of the electrolyte solution is a factor that affects in sensing metal ions as hydrolysis by metal ions would produce more H^+ ions which may block the sites for adsorption in the electrode. Thus it was necessary to investigate the effect of pH in the peak current and consequently, the experiments were conducted by varying the pH from 3.5 to 7 for both Cd^{2+} and Hg^{2+} as for S1(MOF) and S2(MOF) electrodes. As mentioned earlier the DPSV was employed to adjudge the experimental conditions. In fact, for both the cases, peak current attained maximum value at pH=5.5 above which it declines (Fig. 5.6 (a) and (b)). Accordingly, this value of pH has been considered as the optimal value for further experimentation. Like pH the time allowed for the analytes to get accumulated into the electrode plays a crucial role for influencing the peak current. To acquire the best response for S1(MOF) and S2(MOF) electrodes, the accumulation time was varied in between 30 s - 200 s. Here, a gradual increase in current upto 150 s has been witnessed above which the magnitude of current tending to decline for both the electrodes (Fig. 5.6 (c) and (d)). The reason for such a fall can be due to the accumulation of different ions in the electrode causing hindrance to the reaction of the active sites and desired analytes. While taking these experiments into account, an accumulation time of 150 s has been considered for conducting further sensing experiments.

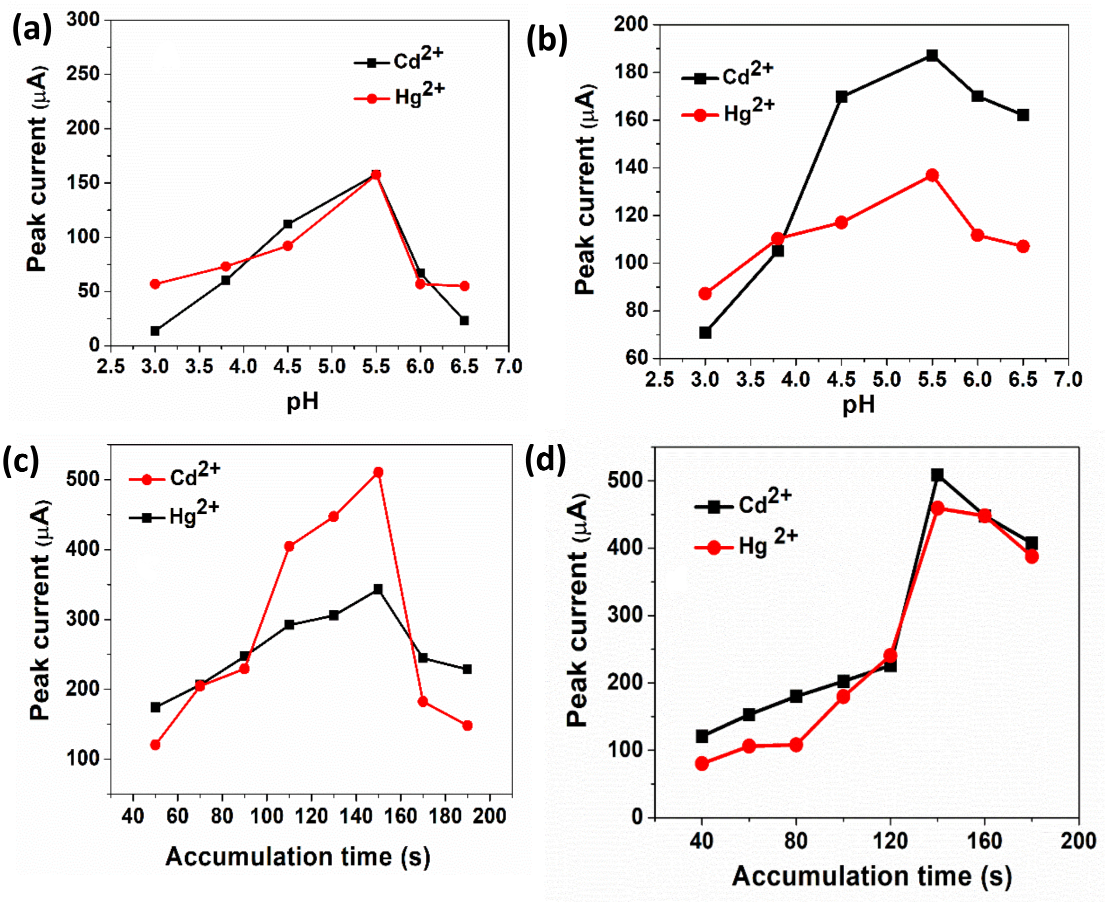

Fig. 5.6 pH vs. peak current of (a) S1(MOF) and (b) S2(MOF) for Cd^{2+} and Hg^{2+}. Accumulation time vs peak current response for detecting Cd^{2+} and Hg^{2+} with reference to samples of (c) S1(MOF) and (d) S2(MOF).

5.4 Electrochemical sensing of Hg^{2+} and Cd^{2+} with S1(MOF) and S2(MOF) coated working electrodes

5.4.1 Individual sensing of Cd^{2+} and Hg^{2+}

For the detection of analytes using S1(MOF) modified ITO electrodes, the DPSV method has been employed in the voltage range of -0.9 to -0.6 V for Cd^{2+} and -0.4 V to 0.4 V for Hg^{2+}. The DPSV curve of S1(MOF) electrode meant for detecting Cd^{2+} in the concentration range of 0.03 μM to 1.2 μM is shown in Fig. 5.7 (a). Here the peaks describe a linear rise in current with concentration given by equation-

$$y = 107x + 138.6, R^2 = 0.9919 \quad (5.4)$$

The limit of detection (LOD) was calculated using the slope of calibration curve (Fig. 5.7 (b) and (d)) following relation:

$$\text{LOD} = 3.3 \times S_y/s\ , \quad (5.5)$$

where S_y is the standard deviation of intercept and s is the slope of the regression plot. The LOD was calculated to be 0.04 μM and with a sensitivity of 107 $\mu A\mu M^{-1}cm^{-2}$ for Cd^{2+}. In a similar way, S1(MOF) electrode was successful in establishing a linear relationship between peak current and concentration for detecting Hg^{2+} over a broad concentration range of 0.06 μM to 1.5 μM represented by the equation-

$$y=237.8x + 76.9,\ R^2=0.9997 \quad (5.6)$$

The LOD for Hg^{2+} is 0.02 μM while sensitivity is relatively higher than the target Cd^{2+} and typically, ~237.8 $\mu A\mu M^{-1}cm^{-2}$ (Fig. 5.7 (c)).

Same experiment was performed for S2(MOF) in the potential range of -1.0 V to -0.2 V for $Cd^{2+}$and -0.4 V to 0.4 V for Hg^{2+}. As can be seen, it could detect Cd^{2+} and Hg^{2+} independently and exhibits a linear increase in peak current with increasing concentration (Fig. 5.8 (a),(c)). For instance, detection of Cd^{2+} in the concentration range of 0.01 μM to 2 μM can be realized through the equation -

$$y=155.5x + 108.5,\ R^2= 0.9987 \quad (5.7)$$

To be mentioned, the LOD and sensitivity were found to be, 0.016 μM and 155.5 $\mu A\mu Mcm^{-2}$; respectively. In a similar manner, the DPSV curve of Hg^{2+} detected by S2 (MOF) has been acquired in the concentration range, 0.02 μM to 1.3 μM, shown in Fig. 5.8 (d). Accordingly, the LOD estimated to be 0.03 μM and sensitivity as, 404.1 μAμM-cm^{-2} predicted from the linear relationship of concentration of analyte and peak current using equation-

$$y= 404.1\ x + 360.7,\ R^2= 0.9995 \quad (5.8)$$

These observations have revealed that both S1(MOF) and S2(MOF) are quite sensitive towards Cd^{2+} and Hg^{2+} but with a higher level of sensitivity for the latter case. To be mentioned, the LODs found by S1(MOF) for Hg^{2+} detection and S2(MOF) for Cd^{2+} detection are lower than the permissible levels set by WHO for drinking water i.e., 3 μg/L ca. 26 nM for Cd^{2+} and 6 μg/L ca. 30 nM for Hg^{2+} [23]. Thus the effectiveness of S1(MOF) and S2(MOF) through exhibition of LODs such as, 14 nM and 24 nM are up to mark and well below the standard set by WHO for Cd^{2+} detection [23]. In contrast, both MOF systems meet the LOD criterion set by WHO standard while sensing Hg^{2+} species. To evaluate the repetabality assay of S1(MOF) and S2(MOF) the experiments were performed on three different electrodes of each, and exhibiting similar linearity trends in Cd^{2+} and Hg^{2+} detection. The standard deviation (SD) of LOD found by all the three electrodes of S1(MOF) in measuring Cd^{2+} and Hg^{2+} was 0.02 and 0.01 (Fig. 5.9 (a) and, (b)). On the other hand, the LOD of S2(MOF) experiences a SD of LOD 0.01 and 0.005 to the detection of Cd^{2+} and Hg^{2+} (Fig. 5.9 (c) and (d)). The results are summarized in Table 5.3.

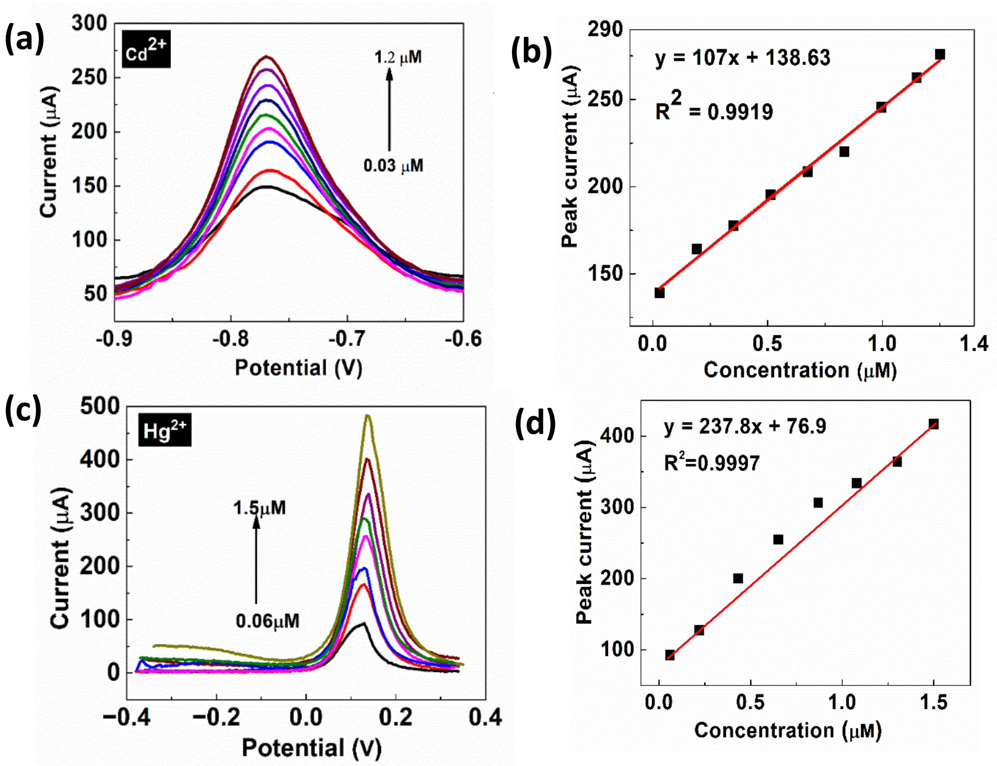

Fig. 5.7 (a) and (c) DPSV results of modified S1(MOF) electrodes for sensing Cd^{2+} and Hg^{2+} individually from concentration 0.03 μM to 1.2 μM and 0.06 μM to 1.5 μM, respectively and (b) and (d) Calibration curve of linear responsivity of peak current with concentration.

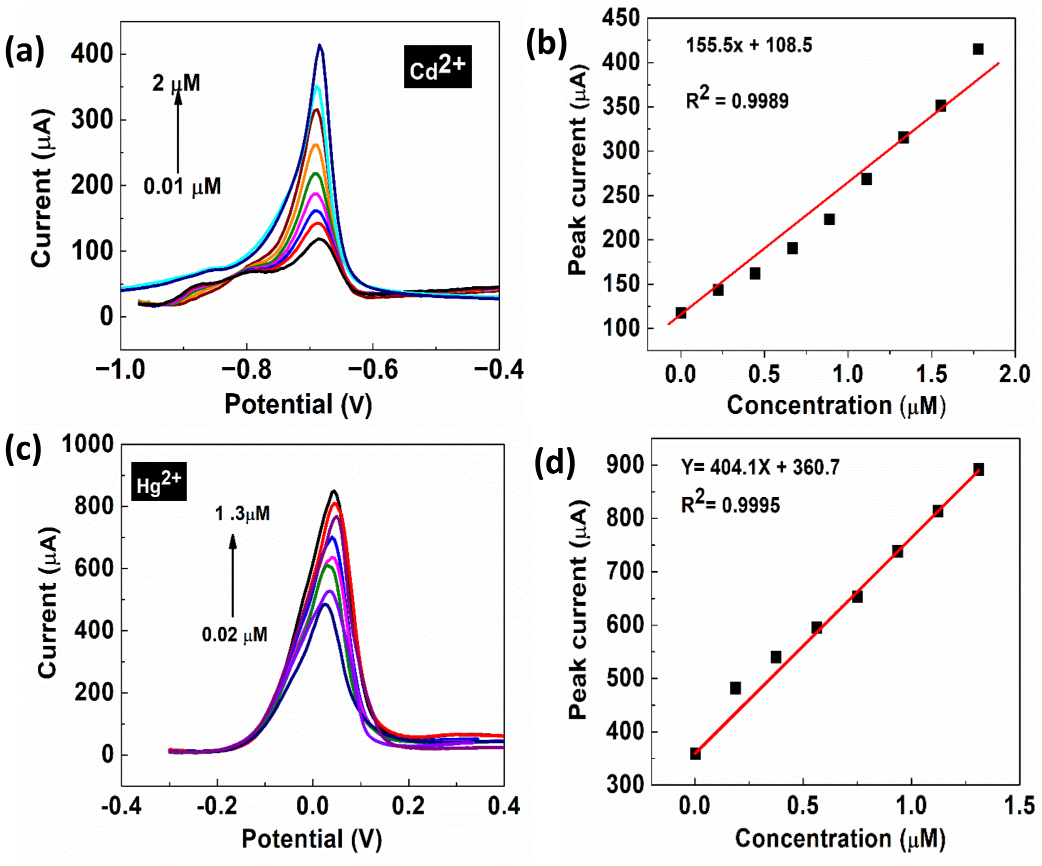

Fig. 5.8 (a) & (c) DPSV results of modified S2(MOF) electrodes for sensing Cd^{2+} and Hg^{2+} individually from concentration 0.01 μM to 2 μM and 0.02 μM to 1.3 μM, respectively and (d) Calibration curve of linear responsivity of peak current with concentration.

Table 5.3 LOD and sensitivity of three electrodes S1(MOF) and S2(MOF) for individual sensing of Cd^{2+} and Hg^{2+}.

Sample		**Parameter**	**Electrode 1**	**Electrode 2**	**Electrode 3**	**SD**
S1(MOF)	**Cd^{2+}**	**LOD (μM)**	0.04	0.021	0.03	0.0095
		Sensitivity (μA)	86.48	107	98.33	9.1
S1(MOF)	**Hg^{2+}**	**LOD (μM)**	0.02	0.015	0.015	0.0028
		Sensitivity (μA)	237.8	258.5	261.8	13.09
S2(MOF)	**Cd^{2+}**	**LOD (μM)**	0.016	0.014	0.016	0.0011
		Sensitivity (μA)	155.5	166.9	148.5	9.28
S2(MOF)	**Hg^{2+}**	**LOD (μM)**	0.03	0.019	0.018	0.0066
		Sensitivity (μA)	404.7	362.48	287.5	59.35

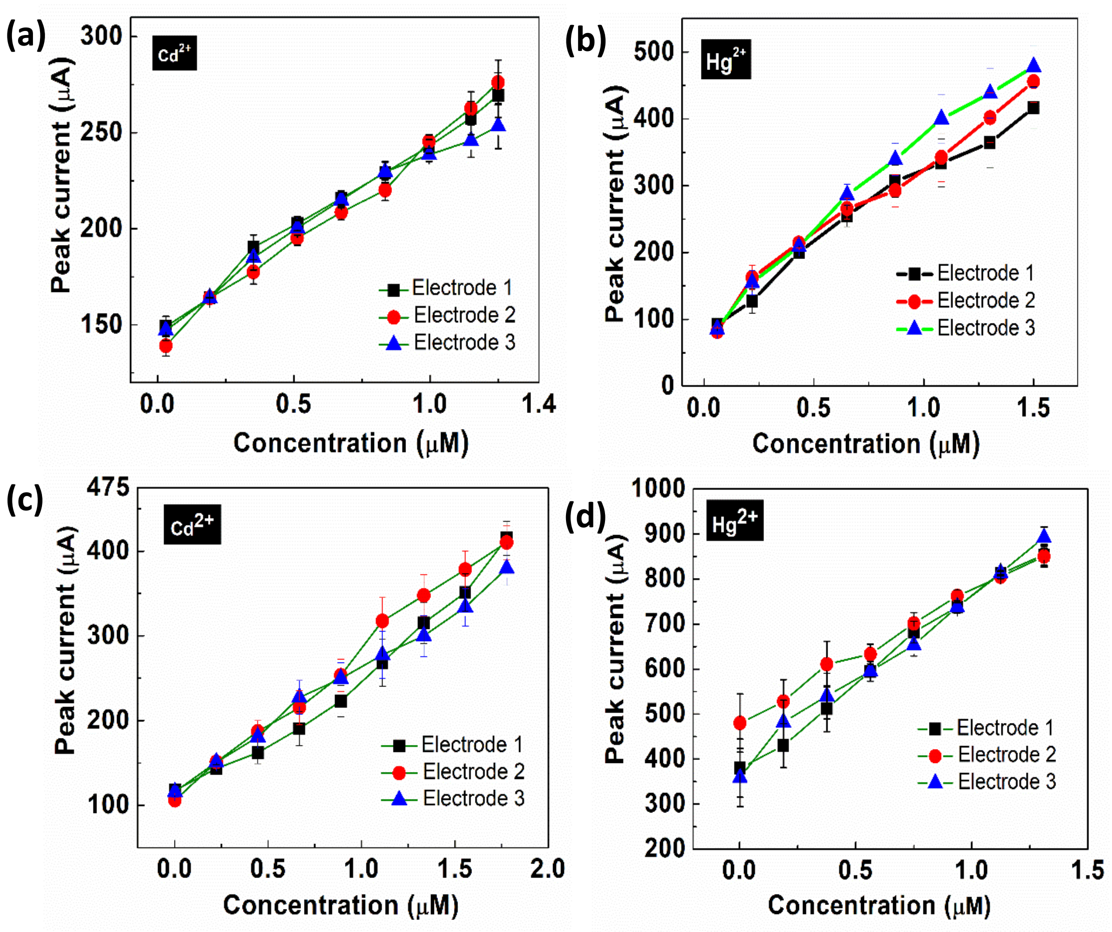

Fig. 5.9 Calibration plot of concentration vs. peak current for (a), (b) S1(MOF) and (c), (d) S2(MOF) while sensing Cd^{2+} and Hg^{2+} with three different working electrodes.

5.4.2 Simultaneous sensing of Cd^{2+} and Hg^{2+} by the electrodes

Later, S1(MOF) and S2(MOF) were tested for simultaneous detection of Cd^{2+} and Hg^{2+}. In the potential range of -1.0 to 0.3 V, S1(MOF) detected Cd^{2+} when the concentration of the analytes varied from 0.05 μM to 1 μM and Hg^{2+} under optimised conditions. Two distinct peaks in the DPSV plot were the consequence of different analytes interacting with various components of S1 (MOF) (Fig. 5.10 (a)). When the concentrations of both analytes increased at the same time, the peak height corresponds to Cd^{2+} and Hg^{2+} increased linearly (Fig. 5.10 (b) and (c)). From the linearity equations shown in 5.10 and 5.11, the LOD values were calculated to be 0.02 μM and 0.001 μM for Cd^{2+} and Hg^{2+} respectively which are lower than their counter parts for the individual detection. The sensitivity of S1(MOF) for Cd^{2+} was found to be 127 μAμM-cm^{-2} and for Hg^{2+} it was 175.8 μAμM-cm^{-2}.

$$y = 187.05\,x + 67.5\,,\ R^2 = 0.9987 \tag{5.10}$$

$$y = 159.1\,x + 6.26\,,\ R^2 = 0.9997 \tag{5.11}$$

The detection procedure for S2(MOF) was considered in a simillar way with the same potential window and same concentration of the analytes. In this case also the peak current increased linearly with increasing concentration of both Cd^{2+} and Hg^{2+} at the same time (Fig. 5.11 (a)). The characteristic empirical relations are given by the equations 5.12 and 5.13 (see Fig. 5.11 (b) and (c)). To be noted, simultaneous detection by S2(MOF) electrode displayed a superior sensitivity feature, for instance, 609.4 µAµM-cm^{-2} for Cd^{2+} and 506.92 µAµM-cm^{-2} for Hg^{2+} in comparison with S1(MOF) one. The electrode S2(MOF) also offered a lower LOD values of 0.01 µM and 0.02 µM for Cd^{2+} and Hg^{2+} respectively (Fig. 5.10 (b)).

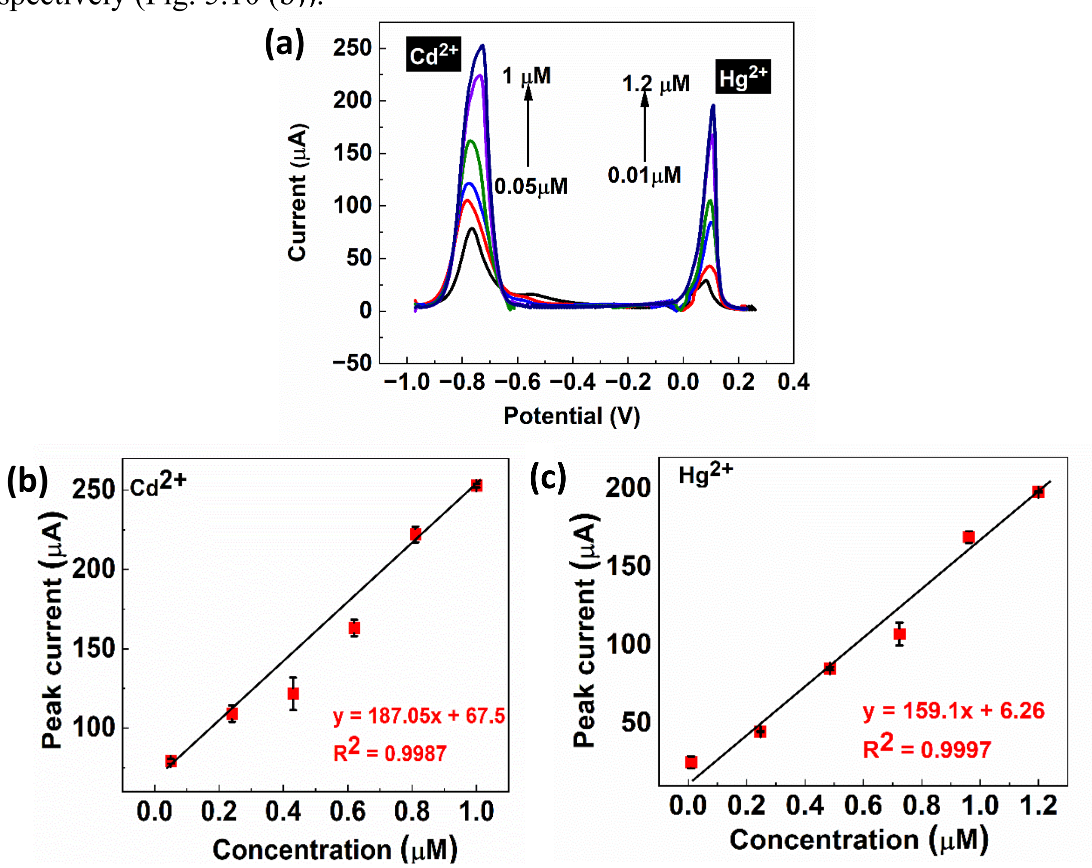

Fig. 5.10 (a) DPSV results of S1(MOF) electrode for sensing Cd^{2+} and Hg^{2+} simultaneously, Calibration curve of concentration vs. peak current for S1(MOF) detecting (b) Cd^{2+} and (c) Hg^{2+}.

Linear relationship of concentration of analytes and peak current while sensing with S2(MOF)

$$y = 551.6\,x + 89.66,\; R^2 = 0.9998 \qquad (5.12)$$

$$y = 341.2x + 98.69,\; R^2 = 0.9999 \qquad (5.13)$$

On performing all the experiments under optimal condition these results draw our attention as the sensing of the same analytes showed varied results in terms of individual and simultaneous detection. During the simultaneous process, a better sensitivity was revealed for both analytes by S2(MOF) electrode than S1(MOF) one. The probable reason for this could be the appropriate exposer of different active sites for the reaction of two different

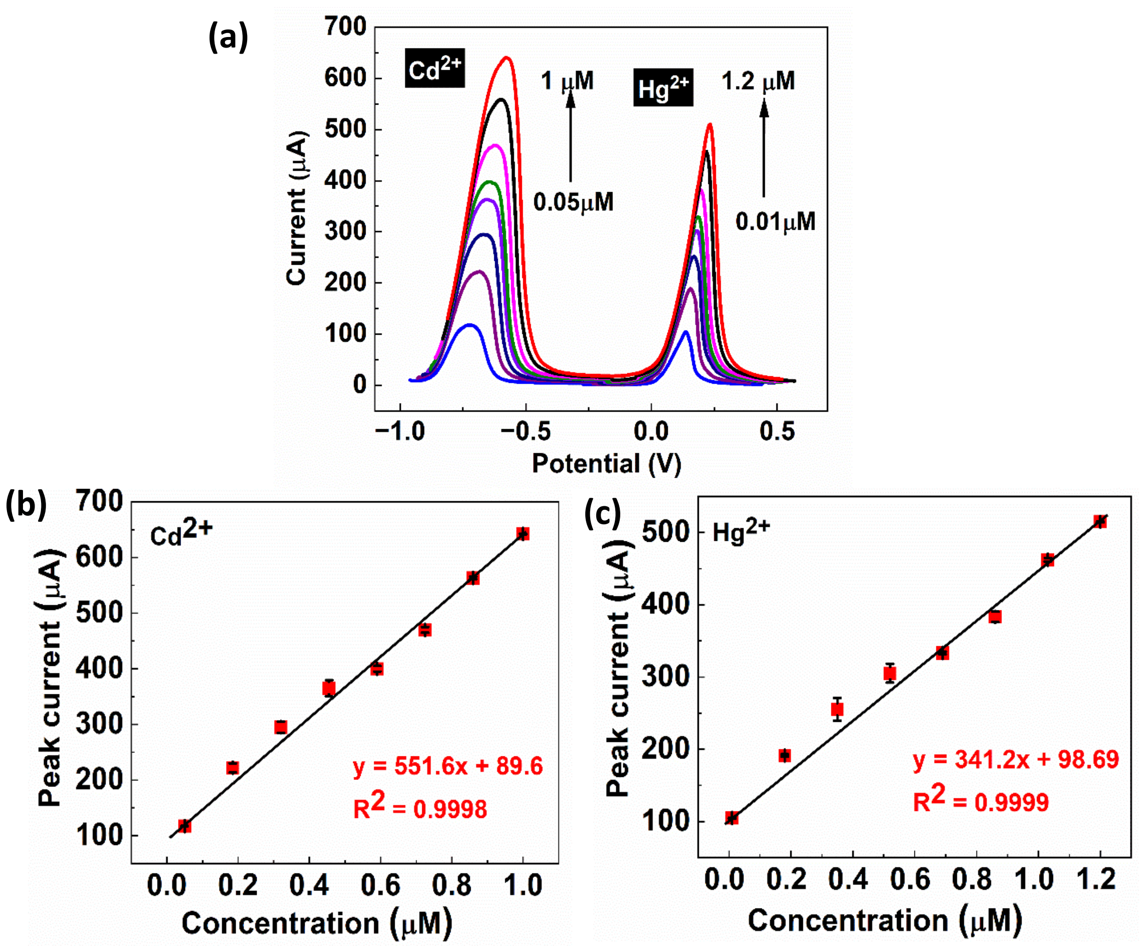

Fig. 5.11 (a) DPSV results of S2(MOF) electrode for sensing Cd^{2+} and Hg^{2+} simultaneously, Calibration curve of concentration vs. peak current for S2(MOF) detecting (b) Cd^{2+} and (c)Hg^{2+}.

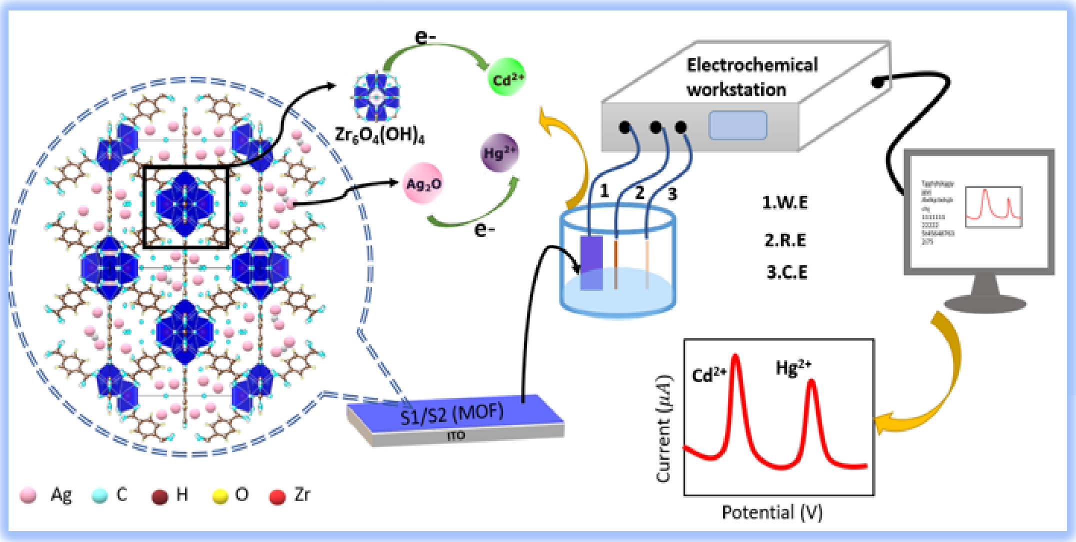

Fig. 5.12 A scheme illustration of Ag_2O–NP decoratd MOF electrode employed for simultaneous electrochemical sensing of Cd^{2+} and Hg^{2+}.

analytes as the Ag_2O NPs present on the surface of UiO-66 are easily accessible to the reactants. On the other hand, S1(MOF) has Ag_2O NPs inside its cavities or within the corethat would make the reaction kinetics sluggish, thereby offering a noticeably lowered sensitivity. The schematic of simultaneous sensing is depicted in Fig. 5.12.

5.4.3 Selectivity study for the electrodes

The selectivity of S1(MOF) and S2(MOF) electrodes was assessed out for various other ions by adding Zn^{2+}, Pb^{2+}, K^+, Fe^{2+} along with 0.05 μM Cd^{2+} and Hg^{2+} in the PBS solution. All the other ions added in the solution are needed to check their response on the detection efficiency of the prepared electrodes while undertaking simultaneous sensing of Cd^{2+} and Hg^{2+}. To be mentioned, the interfering ions were added with a higher concentration (100 times more) than the analytes of our interest. Fig. 5.13 (a) and (b) showed the DPSV patterns of S1(MOF) and S2(MOF) after introducing other metal ions, which in fact, characterize sharp peaks only for Cd^{2+} and Hg^{2+} and without any obvious peaks for Zn^{2+}, Pb^{2+}, K^+, Fe^{2+} etc. This result is indicative towards the selectivity of S1(MOF) and S2(MOF) for Cd^{2+} and Hg^{2+}. To find out the reason behind the selectivity of our working

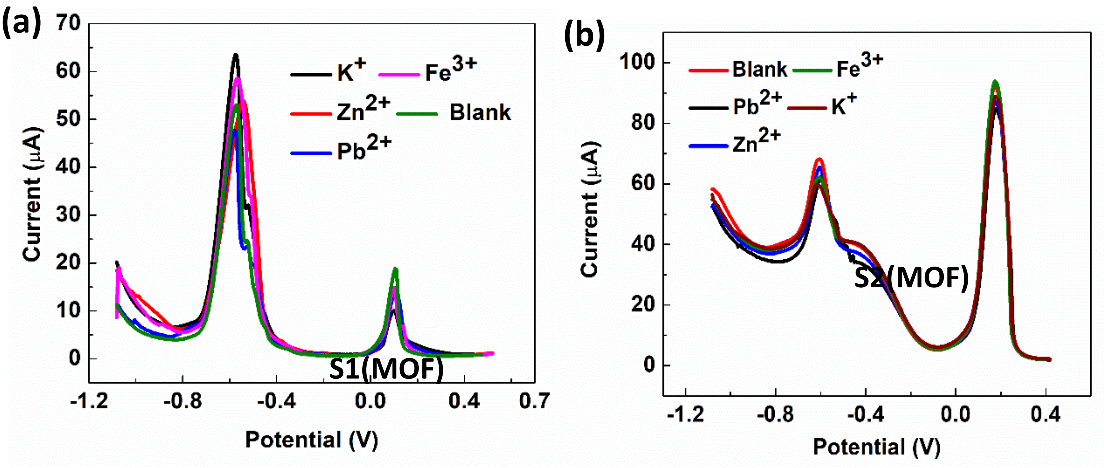

Fig. 5.13 DPSV of (a) S1(MOF), (b) S2(MOF) in the absence and presence of interfering metal ions Fe^{3+}, Pb^{2+}, K^{+}, and Zn^{2+}.

electrodes, the DPSV of Ag_2O and UiO-66 was performed for Cd^{2+} and Hg^{2+} which revealed the fact that bare UiO-66-MOF can detect Cd^{2+}. Thus, it not only provides the adsorption site but also takes part in the redox reaction. Moreover, access to Zr present in MOF takes part in the reduction process of Cd^{2+} in accordance with the work of Ding and co-workers [10]. Similarly, Ag_2O NPs also offer characteristic peaks which are attributed to the oxygen reduction and Ag^{+} oxidation peak that would occur during electron donation to Hg^{2+}.

5.4.4 Stability and reproducibility features of the electrodes

Stability and reproducibility are important parameters for a sensor material to be established as a promising sensor. Therefore, to observe the stability and repeatability holds of our prepared working electrodes the DPSV data were recorded several times with 0.05 μM Cd^{2+} and Hg^{2+} solutions for both S1(MOF) and S2(MOF) for optimal effects (Fig. 5.14 (a),(b)). From these tests, the respective standard deviation in the peak currents were predicted as, 9.35 μA and 8.3 μA for Cd^{2+} and Hg^{2+} when detected by the first electrode, whereas the second working electrode gave 3.66 μA and 4.66 μA upto ten cycles . Even though after ten cycles peak current declines gradually the electrodes remain stable upto twenty cycles. From these observations, S1(MOF) was believed to be relatively more stable than S2(MOF) one.

To examine the reproducibility of six electrodes of S1(MOF) prepared in the same batch they were taken for the DPSV meaurements in PBS solution with 0.5 µM concentration of Cd^{2+} and Hg^{2+}. All the six electrodes showed closely similar responses with a relative standard deviation of 9 µA in Hg^{2+} and 5.7 µA in Cd^{2+}. Conversely, 6 electrodes of S2(MOF) from the same lot were checked for reproducibility in PBS with 0.5 µM concentrations of Cd^{2+} and Hg^{2+}. It is worth mentioning here that, in terms of reproducibility the S2(MOF) is superior to its counterpart as the former has lower standard deviation for six samples such as, 11.4 µA for Cd^{2+} and 10.6 µA – for Hg^{2+} as depicted in Fig. 5.14 (c) and (d).

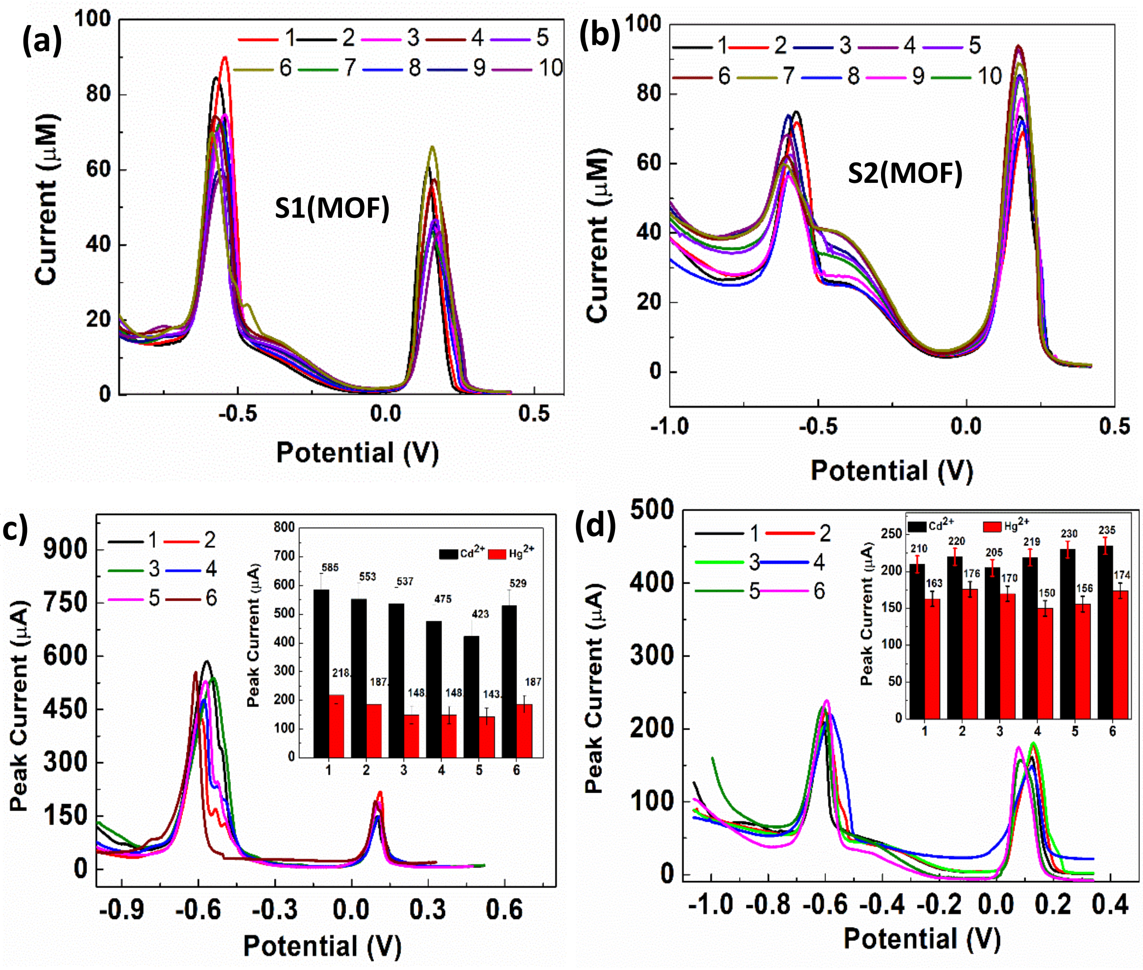

Fig. 5.14 Stability and repeatability experiments of (a) S1(MOF) and (b) S2(MOF) upto 10 cycles, The DPSV patterns of (c) S1(MOF) and (d) S2(MOF) sensing Cd^{2+} and Hg^{2+} simultaneously in 6 different electrodes to check the reproducibility.

5.4.5 Real sample analysis

The feasibility of the presented electrodes in simultaneous detection of Cd^{2+} and Hg^{2+} has been examined in real water samples. In this regard, lake water collected from our university campus has been tested employing electrochemical methods. No DPSV response has been observed in the lake water samples, revealing either non-availability, or a lower concentration of the analytes, below the detection limit. Employing the standard procedure, 0.1 μM standard solution of Cd^{2+} and Hg^{2+} are spiked into the real sample. As tabulated in Table 5.4. the recoveries of Cd^{2+} using S1(MOF) and S2(MOF) are 81.36 % and 101.4 %, respectively. In Hg^{2+} detection, recoveries were found 78.71 % for S1 (MOF) and 95.66% for S2(MOF) (Table 5.4). These results are quite evident for these electrodes to be useful in the real-life applications.

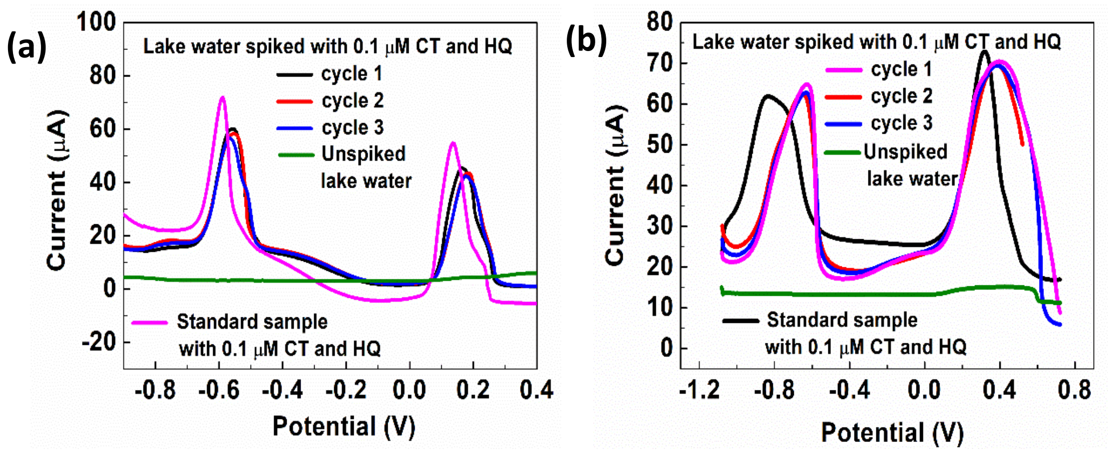

Fig. 5.14 Detection of Cd^{2+} and Hg^{2+} when spiked in lake water sample by (a) S1(MOF) and (B) S2(MOF).

Table 5.4 Results of Cd^{2+} and Hg^{2+}detection in local lake water sample by S1(MOF) and S2(MOF)

Sample	Detected (μmol. L^{-1})		Added (μmol. L^{-1})		Total (μmol. L^{-1})		Recovery (%)		RSD (%)	
	Cd^{2+}	Hg^{2+}	Cd^{2+}	Hg^{2+}	Cd^{2+}	Hg^{2+}	Cd^{2+}	Hg^{2+}	Cd^{2+}	Hg^{2+}
Lake water-S1(MOF)	0.0	0.0	0.1	0.1	0.094±0.002	0.07± 0.001	81.36	78.71	2.82	3.2
Lake water-S2(MOF)	0.0	0.0	0.1	0.1	0.1±0.0015	0.09± 5.E-4	101.4	95.66	2.91	0.36

Table 5.5 Comparision of sensing properties of S1(MOF) and S2(MOF) electrodes with some previously reported sensors of Cd^{2+} and Hg^{2+}.

Electrode	**Sensitivity** μA·μM⁻¹·cm⁻²		**Limit of detection** (μM)		**Reference**
	Cd^{2+}	Hg^{2+}	Cd^{2+}	Hg^{2+}	
ZIF-8-CS	1.390	14.20	0.135	0.0293	[1]
MIL-100(Cr)	-	-	0.04	-	[2]
MIL-47(as)/CPE	-	-	-	0.067	[3]
GA-UiO-66-NH_2	-	-	0.02	0.002	[4]
Au/ZIF67	-	114.3	-	0.002	[5]
ZIF-67	-	-	0.0011	0.0012	[6]
Iron oxide on ZIF-67.	41.5	-	0.0078	-	[7]
S1(MOF)*- (individual)	107	222.97	0.04	0.04	*This work*
S2(MOF)*- individual	155.5	404.1	0.016	0.03	*This work*
S1(MOF)-simultaneous	187.05	159.1	0.05	0.02	*This work*
S2(MOF)-simultaneous	551.6	341.2	0.008	0.003	*This work*

5.5 Conclusions

In this chapter, the two composites of Zr-based MOF UiO-66 and Ag_2O NPs prepared through two different synthesis routes were studied for their electrochemical behaviour and sensing applications. The electrochemical performance of S1(MOF) and S2(MOF) coated on ITO glass were carried out in an aqueous electrolyte of 0.1 M PBS via CV and EIS. When compared to bare ITO and UiO-66, the CV and EIS results showed that S1(MOF) and S2(MOF) had improved electroactivity with a clear pair of redox peaks. However, in terms of charge transfer resistance and current responsiveness, the second electrode performed better. The sensing performance of both S1(MOF) and S2(MOF) has been carried out for two analytes namely, Hg^{2+} and Cd^{2+} independently and simultaneously. Both S1(MOF) and S2(MOF) offered higher sensitivity towards the analytes as compared to the earlier reports (Table. 5.5). The sensitivity of S2(MOF) towards both the heavy metal ions under study seemed to be almost equal when sensing was considered on individual and simultaneous basis. When monitored Hg^{2+} and Cd^{2+} simultaneously, the S2(MOF) electrode could detect analytes upto nM concentration which is lower than the permissible concentration for Hg^{2+} and Cd^{2+} in drinking water recommended by WHO. These results lead us to a conclusion that UiO-66 MOFs decorated with Ag_2O NPs through natural reducing agent can be a better sensing material for simultaneous detection which has the advantage of adopting a greener synthesis and superior performance. Looking into the behaviour of these materials the electrodes under study can have immense scope for practical applications in the near future.

References

[1] Vargas, GH., Hernández, JES., Hernandez, SS., Rodríguez, AMV., Saldivar, RP., Iqbal, HMN. Electrochemical Biosensors: A Solution to Pollution Detection with Reference to Environmental Contaminants. *Biosensors*, ***28*** :29, 2018.

[2] Malik, LA., Bashir, A., Qureashi, A., Pandith, AH., Detection and removal of heavy metal ions: a review. *Environ. Chem. Lett.* **17**:1495–1521, 2019.

[3] Wu, Y.,_Pang, H., Liu, Y., Wang, X., Yu, S., Fu, D., Chen, J., Wang, X., Environmental remediation of heavy metal ions by novel-nanomaterials: *A review. Environ. Pollut.* **246**:608-620, 2019.

[4] Cui, L., Wu, J., Ju ,W., Electrochemical sensing of heavy metal ions with inorganic, organic and bio-materials. *Biosens. Bioelectron* **63**:276-286, 2015.

[5] Noviana, E., , McCord, CP. , Clark, KM. , Jang, I. , Charles, SH., Electrochemical paper-based devices: sensing approaches and progress toward practical applications. *Lab Chip* **20**: 9-34, 2020.

[6] Kempahanumakkagari, S., Vellingiri, K., Deep, A., Kwon, E.,_Bolan, N., Kim, K ., Metal–organic framework composites as electrocatalysts for electrochemical sensing applications. *Coord. Chem. Rev.* **375** :105-129, 2018

[7] Butova, V V., Soldatov, M A., Guda, A A, Lomachenko, K A. and Lamberti, C ., Metal-organic frameworks: structure, properties, methods of synthesis and characterization. *Russ. Chem. Rev.* **85**: 280, 2016

[8] Dawei, Xu., Cong, Li., Yuqiu, Zi., Dafeng, Jiang., Fei, Qu. and Xian-En, Zhao., MOF@MnO_2 nanocomposites prepared using in situ method and recyclable cholesterol oxidase-inorganic hybrid nanoflowers for cholesterol determination. *Nanotechnology* **32**:315502,2021.

[9] Peixin, Liu., Peng, Jing., Xuan, Xu., Baocang, Liu. and Jun, Zhang., Structural Reconstruction of Ce-MOF with Active Sites for Efficient Electrocatalytic N_2 Reduction. *ACS Appl. Energy Mater.* **4**: 12128–12136, 2021

[10] Liu, Y., Wu, S., Xiong, W., Li, H., Interface Co-Assembly Synthesis of Magnetic Fe_3O_4@mesoporous Carbon for Efficient Electrochemical Detection of Hg (II) and Pb (II). *Advance Materials Interfaces*. **10**:2201631, 2022.

[11] Wu, S., Xiong, W., Li, Hao. Insights into the Fe oxidation state of sphere-like Fe_2O_3 nanoparticles for simultaneous Pb^{2+} and Cu^{2+} detection. *Journal of Alloys and Compounds* **934**:167863, 2023.

[12] Xiong, W., Zhang, P., Liu, S., Lv ,Y., Zhang, D., Catalyst-free synthesis of phenolic-resin-based carbon nanospheres for simultaneous electrochemical detection of Cu (II) and Hg (II). *Diamond and Related Materials* **111** :108170, 2021.

[13] Ding, Y., Wei, F., Dong, C., Li, J., Zhang, C., Li, X.H., UiO-66 based electrochemical sensor for simultaneous detection of Cd (II) and Pb (II). *Inorg. Chem. Commun.* **131**:108785, 2021.

[14] Lu, M., Deng, Y., Luo, Y., Lv, J., Li, T., Xu, J., Chen, S W. and Wang, J., Graphene Aerogel−Metal−Organic Framework-Based Electrochemical Method for Simultaneous Detection of Multiple Heavy-Metal Ions. *Anal. Chem*. **9**: 888−895, 2019.

[15] Zhang, X., Song, L,Bi Fu., Zhang, D., Wang, Y., Cui, L., Catalytic oxidation of toluene using a facile synthesized Ag nanoparticle supported on UiO-66 derivative. *Journal of Colloid and Interface Science* **571**:38–47, 2020.

[16] Li, Y.X., Wei, Z.Y., Liu, L., Gao, M.L., Han, Z.B., Ag nanoparticles supported on UiO-66 for selective oxidation of styrene. *Inorg. Chem. Commun*. 88:47–50, 2018.

[17] Sun, Z.G., Li, G., Zhang, Y., Liu, H.O., Gao, X.H., 2015 Ag–Cu–BTC prepared by post synthetic exchange as effective catalyst for selective oxidation of toluene to benzaldehyde. *Catal. Commun*. **59**: 92–96, 2015.

[18] Han, C., Yang, J., Gu, J., Immobilization of silver nanoparticles in Zr-based MOFs: induction of apoptosis in cancer cells. *J Nanopart. Res.* **20**:77, 2018.

[19] Brown, A., Anson, F., Cyclic and differential pulse voltametric behaviour of reactants confined to the electrode surface. *Analytical Chemistry*. **49**: 1589-1595, 1977.

[20] Liu, W., Huang, B., Zheng, L., Shen, M., Pu, Z., Shao, Y., Li, X., Liao, S., UiO-66-NH_2-derived mesoporous carbon used as a high-performance anode for the potassium-ion battery. *RSC Adv.* **11**:1039-1049, 2021.

[21] Allen, J., Bard, and Larry, R., Faulkner, "Electrochemical Methods: Fundamentals and Applications" (2nd ed.) *John Wiley & Sons*. ISBN 0-471-04372-9, 2001.

[22] Medhi, A., Baruah, S., Singh., J, Betty, CA., Mohanta D. Au nanoparticle modified GO/PEDOT-PSS based immunosensor probes for sensitive and selective detection of serum immunoglobulin G (*IgG*). *Appl. Surf. Sci.* **575**:151775, 2022.

[23] Guidelines for drinking-water quality: fourth edition incorporating the first and second addenda. Geneva: World Health Organization; Licence: CC BY-NC-SA 3.0 IGO 2022.